REPORT

LIQUID CRYSTALS

Topological structure and dynamics of three-dimensional active nematics

Guillaume Duclos[1]*, Raymond Adkins[2]*, Debarghya Banerjee[3,4], Matthew S. E. Peterson[1], Minu Varghese[1], Itamar Kolvin[2], Arvind Baskaran[1], Robert A. Pelcovits[5], Thomas R. Powers[6,5], Aparna Baskaran[1], Federico Toschi[7,8], Michael F. Hagan[1], Sebastian J. Streichan[2], Vincenzo Vitelli[9], Daniel A. Beller[10]†, Zvonimir Dogic[1,2]†

Topological structures are effective descriptors of the nonequilibrium dynamics of diverse many-body systems. For example, motile, point-like topological defects capture the salient features of two-dimensional active liquid crystals composed of energy-consuming anisotropic units. We dispersed force-generating microtubule bundles in a passive colloidal liquid crystal to form a three-dimensional active nematic. Light-sheet microscopy revealed the temporal evolution of the millimeter-scale structure of these active nematics with single-bundle resolution. The primary topological excitations are extended, charge-neutral disclination loops that undergo complex dynamics and recombination events. Our work suggests a framework for analyzing the nonequilibrium dynamics of bulk anisotropic systems as diverse as driven complex fluids, active metamaterials, biological tissues, and collections of robots or organisms.

The sinuous change in the orientation of birds flocking is a common but startling sight. Even if one can track the orientation of each bird, making sense of such large datasets is difficult. Similar challenges arise in disparate contexts from magnetohydrodynamics (*1*) to turbulent cultures of elongated cells (*2*), where oriented fields coupled to velocity undergo complex dynamics. To make progress with such extensive three-dimensional (3D) data, it is useful to identify effective degrees of freedom that allow a coarse-grained description of the collective nonequilibrium phenomena. Promising candidates are singular field configurations locally protected by topological rules (*3*–*9*). Examples of such singularities in 2D are the topological defects that appear at the north and south poles when covering the Earth's surface with parallel lines of longitude or latitude. These point defects are characterized by the winding number of the corresponding orientation field.

The quintessential systems with orientational order are nematic liquid crystals, which are fluids composed of anisotropic molecules. In equilibrium, nematics tend to minimize energy by uniformly aligning their anisotropic constituents, which annihilates topological defects. By contrast, in active nematic materials, which are internally driven away from equilibrium, the continual injection of energy destabilizes defect-free alignment (*10*, *11*). The resulting chaotic dynamics are effectively represented in 2D by point-like topological defects that behave as self-propelled particles (*12*–*16*). The defect-driven dynamics of 2D active nematics have been observed in many systems ranging from millimeter-sized shaken granular rods and micrometer-sized motile biological cells to nanoscale motor-driven biological filaments (*17*–*23*). Several obstacles have hindered generalizing topological dynamics of active nematics to 3D. The higher dimensionality expands the space of possible defect configurations. Discriminating between different defect types requires measurement of the spatiotemporal evolution of the director field on macroscopic scales using materials that can be rendered active away from surfaces.

The 3D active nematics that we assembled are based on microtubules and kinesin molecular motors. In the presence of a depleting agent, these components assemble into isotropic active fluids that exhibit persistent spontaneous flows (*17*). Replacing a broadly acting depletant with a specific microtubule cross-linker, PRC1-NS, enabled assembly of a composite mixture of low-density extensile microtubule bundles (~0.1% volume fraction) and a passive colloidal nematic based on filamentous viruses (Fig. 1A), a strategy that is similar to work on the living liquid crystal (*21*). Adenosine 5′-triphosphate (ATP)–fueled stepping of kinesin motors generates microtubule bundle extension and active stresses that drive the chaotic dynamics of the entire system (movie S1). Birefringence of the composite material indicates local nematic order (Fig. 1B), in contrast to active fluids lacking the passive liquid crystal component.

Elucidating the spatial structure of a 3D active nematic requires measurement of the nematic director field on scales from micrometers to millimeters. Furthermore, uncovering its dynamics requires acquisition of the director field with high temporal resolution. To overcome these constraints, we used a multiview light sheet microscope (Fig. 1C) (*24*). The spatiotemporal evolution of the nematic director field $\mathbf{n}(x,y,z,t)$ was extracted from a stack of fluorescent images using the structure tensor method. Spatial gradients of the director field identified regions with large elastic distortions (Fig. 1D and movie S2). Three-dimensional reconstruction of such maps revealed that large elastic distortions mainly formed curvilinear structures, which could either be isolated loops or belong to a complex network of system-spanning lines (Fig. 1E and movie S3). These curvilinear distortions are topological disclination lines characteristic of 3D nematics. Similar structures were observed in numerical simulations of 3D active nematic dynamics using either a hybrid lattice Boltzmann method or a finite difference Stokes solver numerical approach (Fig. 1F) (*25*, *26*).

Reducing the ATP concentration slowed down the chaotic flows, which revealed the temporal dynamics of the nematic director field. In turn, this identified the basic events governing the dynamics of disclination lines (movie S4). We focused on characterizing the closed loop disclinations because they are the objects seen to arise or annihilate in the bulk. Isolated loops nucleated and grew from undistorted, uniformly aligned regions (Fig. 2A, figs. S1 and S2, and movie S5). Likewise, loops also contracted and self-annihilated, leaving behind a uniform region (Fig. 2B, figs. S1 and S2, and movie S6). Furthermore, expanding loops frequently encountered and subsequently merged with the system-spanning network of distortion lines, whereas the distortion lines in the network self-intersected and reconnected to emit a new isolated loop (Fig. 2, C and D; figs. S1 and S2; and movies S7 and S8).

Topological constraints require that topological defects can only be created in sets that are, collectively, topologically neutral. Point-like defects in 2D active nematics thus always nucleate as pairs of opposite winding number (*13*). In 3D active nematics, an isolated disclination loop as a whole has two topological possibilities: It can either carry a

[1]Department of Physics, Brandeis University, Waltham, MA 02453, USA. [2]Department of Physics, University of California, Santa Barbara, CA 93111, USA. [3]Max Planck Institute for Dynamics and Self-Organization, 37077 Göttingen, Germany. [4]Instituut-Lorentz, Universiteit Leiden, 2300 RA Leiden, Netherlands. [5]Department of Physics, Brown University, Providence, RI 02912, USA. [6]School of Engineering, Brown University, Providence, RI 02912, USA. [7]Department of Applied Physics, Eindhoven University of Technology, 5600 MB Eindhoven, Netherlands. [8]Instituto per le Applicazioni del Calcolo CNR, 00185 Rome, Italy. [9]James Frank Institute and Department of Physics, The University of Chicago, Chicago, IL 60637, USA. [10]Department of Physics, University of California, Merced, CA 95343, USA.
*These authors contributed equally to this work.
†Corresponding author. Email: dbeller@ucmerced.edu (D.A.B.); zdogic@ucsb.edu (Z.D.)

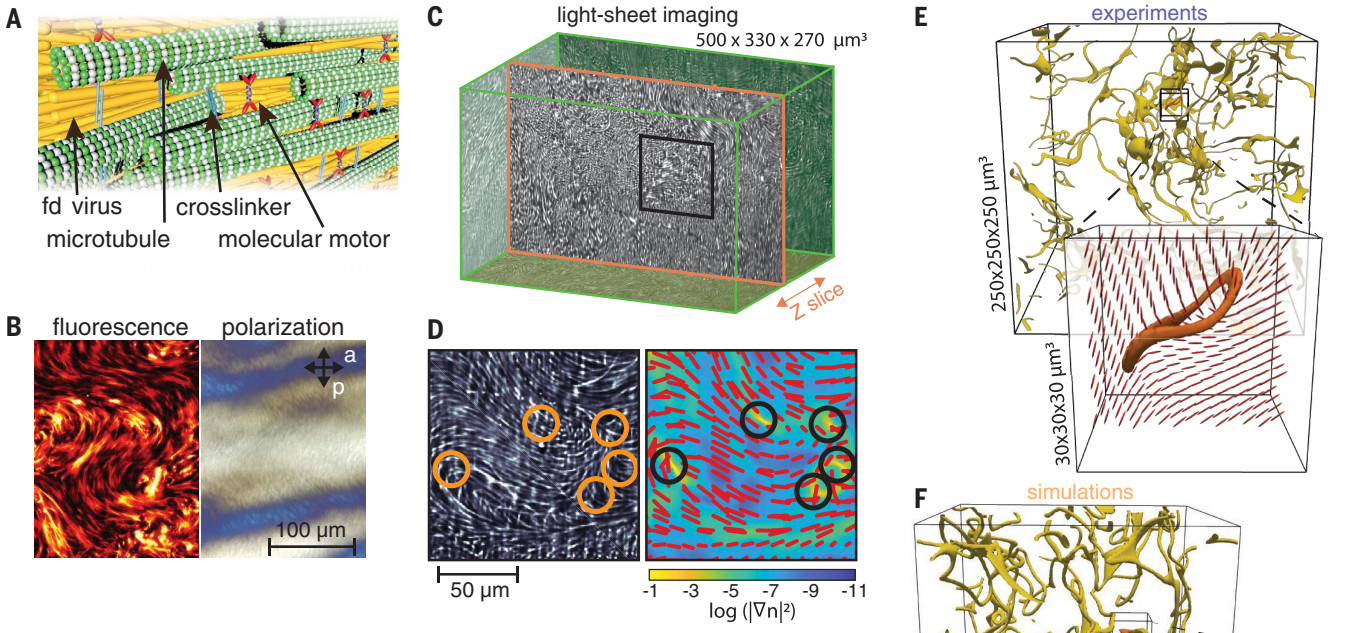

Fig. 1. Assembling 3D active nematics and imaging their director field. (**A**) Schematic of the 3D active nematic system: active stress–generating extensile microtubule bundles are dispersed in a passive colloidal liquid crystal. (**B**) Active 3D nematic imaged with widefield fluorescent microscopy (left) and polarized microscopy (right). Birefringence indicates local nematic order. (**C**) Multiview light sheet microscopy allows for 3D imaging of millimeter-sized samples with single-bundle resolution. (**D**) Left: A 2D slice of fluorescent microtubule bundles with highlighted elastic distortions. Right: Corresponding elastic distortion energy map, with an overlaid nematic director field (red). (**E**) Three-dimensional elastic distortion map revealing the presence of curvilinear rather than point-like singularities. An entangled network of lines coexists with isolated loops. (**F**) Hybrid lattice Boltzmann simulations yield a similar structure of 3D active nematics. All experimental samples consist of passive *fd* viruses at 25 mg/mL and microtubules at 1.33 mg/mL.

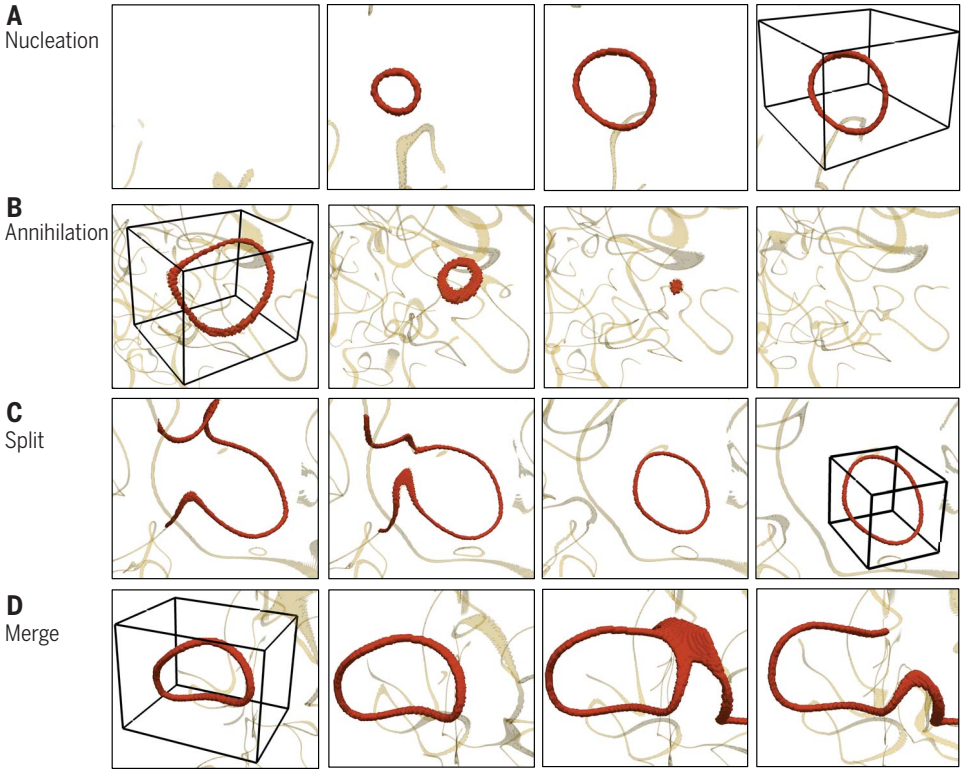

Fig. 2. Dynamics of experimentally observed disclination loops. (**A**) Loop nucleation from a defect-free region. (**B**) Loop self-annihilation leaves behind a defect-free nematic. (**C**) Disclination line self-intersects, reconnects, and emits a loop. (**D**) Disclination loop intersects, reconnects, and merges with a disclination line. Each bounding box is 30 × 30 × 38 μm. The time interval between two pictures is 12 s.

monopole charge or be topologically neutral, depending on its director winding structure. Because charged topological loops can only appear in pairs, nucleation of isolated loops as observed in our system implies their topological neutrality.

To establish that the closed-loop distortions are nematic disclination loops with no net charge, we characterized their topological structure. In 2D nematics, point-like disclination defects are characterized by the winding number or topological charge(s). The lowest-energy disclinations have $s = \pm 1/2$, which corresponds to a π rotation of the director field in the same sense or the opposite sense, respectively, as the traversal of any closed path encircling only the defect of interest. In 3D nematics, point-like defects

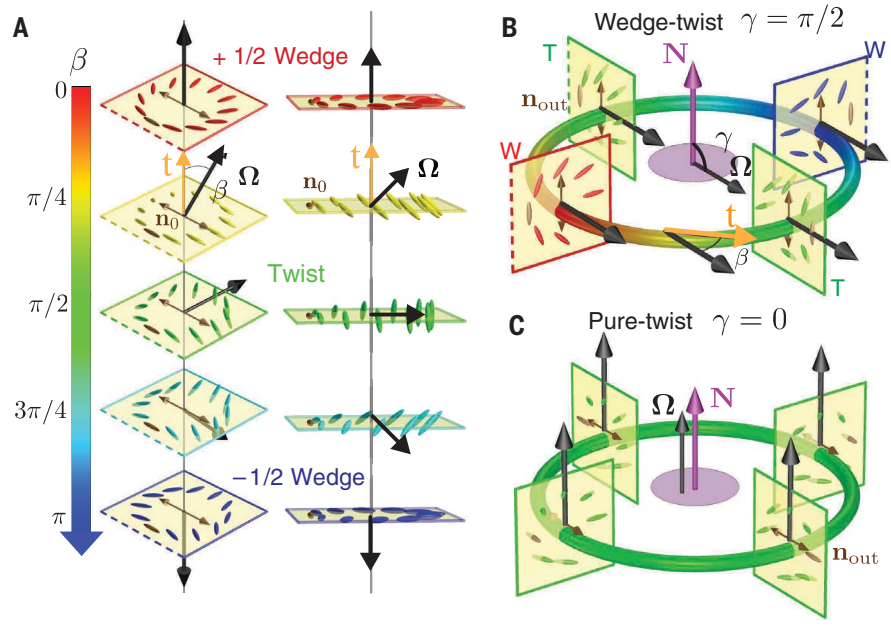

Fig. 3. Structure of disclinations lines, wedge-twist, and pure-twist loops. (**A**) Disclination line where a local +1/2 wedge winding continuously transforms into a −1/2 wedge through an intermediate twist winding. The director field winds by π about the rotation vector $\boldsymbol{\Omega}$ (black arrows), which makes angle β with the tangent **t** (orange arrow) and is orthogonal to the director field everywhere in each slice. For ±1/2 wedge windings, $\beta = 0$ and π. $\beta = \pi/2$ indicates local twist winding. Reference director $\mathbf{n_o}$ (brown) is held fixed. Color map indicates angle β. (**B**) Wedge-twist loop where local winding as reflected by angle β varies along the loop. $\boldsymbol{\Omega}$ is spatially uniform and forms an angle $\gamma = \pi/2$ with the loop's normal, **N**. The winding in the four illustrated planes corresponds to the profiles of the same colors shown in (A), with dashed edges of squares aligned to match the local director field. Double-headed brown arrows indicate $\mathbf{n_{out}}$, the director just outside the loop. (**C**) Pure-twist loop, with $\boldsymbol{\Omega}$ both uniformly parallel to loop normal **N** ($\gamma = 0$) and perpendicular to the tangent vector.

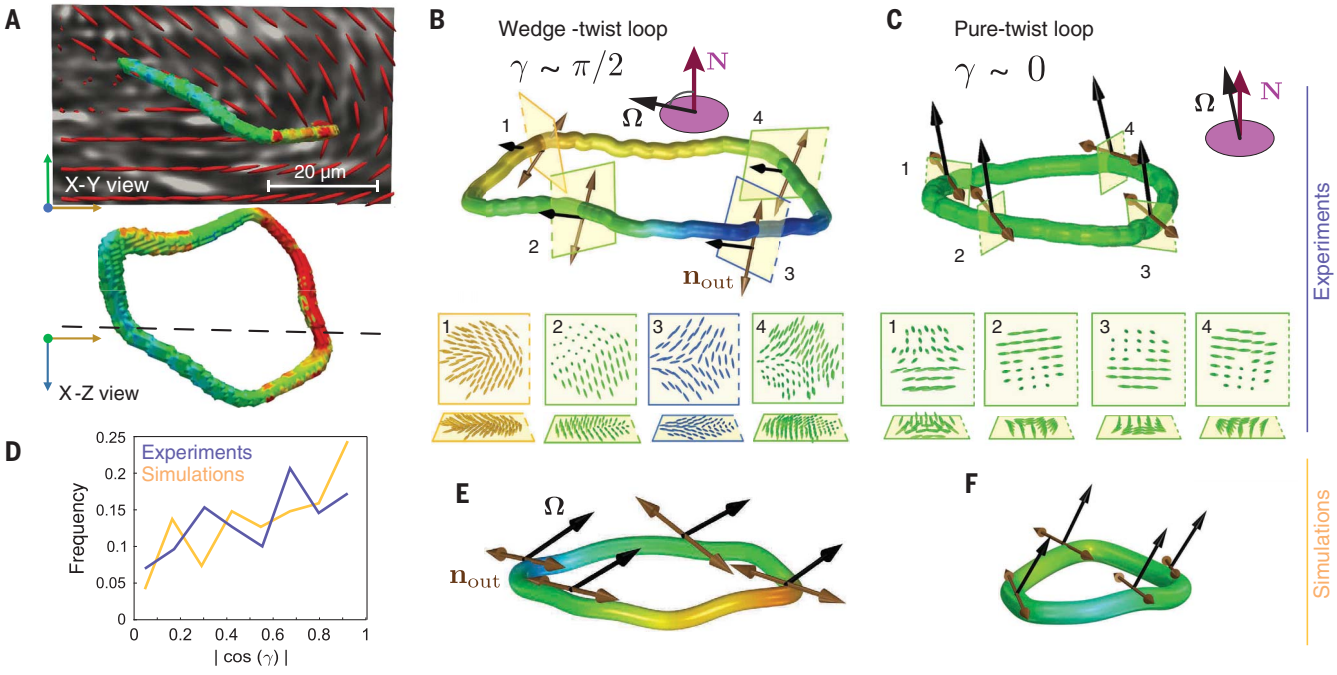

Fig. 4. Structure of disclination loops in experiments and theory. (**A**) Two orthogonal views of an experimental wedge-twist loop overlaid onto a fluorescent image of the microtubules. The nematic director is shown in red. (**B** and **E**) Structure of wedge-twist disclination loops in experiments and simulation. (**C** and **F**) Structure of pure-twist disclination loops from experiment and simulation. Panels show the director field's winding in the corresponding cross-sections on the experimental loops. (**D**) Distribution of loop types extracted from experiment ($N = 268$) and hybrid lattice Boltzmann simulations ($N = 94$). $|\cos(\gamma)| = 0$ for wedge-twist loops and 1 for pure-twist loops. Distributions of standard deviations of $|\cos(\gamma)|$ are shown in fig. S3. The count of simulated loops includes analysis of some loops at multiple time points because we did not track loop identity in the complex flow dynamics. Coloring of loops indicates the angle β. Scales and bounding boxes for the loops are shown in fig. S4.

from 2D systems are generalized to disclination lines, where the director similarly has a π winding, affording a broader variety of director configurations. We define **t** to be the disclination line's local tangent unit vector. The director field winds by π about a direction specified by **Ω**, the rotation vector, which can make an arbitrary angle β with **t** (*27*). If **Ω** points antiparallel or parallel to **t**, then the local director field rotates in the plane orthogonal to **t**, assuming the disclination profiles familiar from 2D nematics. These configurations in which β is equal to 0 or π are said to have a local wedge winding (Fig. 3A). If **Ω** is perpendicular to **t**, then β = π/2 and the director forms a spatially varying angle away from the orthogonal plane, locally creating what is called a twist winding. Because **Ω** may point in any direction relative to **t**, both **Ω** and β can vary continuously along a disclination line (movie S9).

For disclination lines forming loops, **Ω** can vary continuously providing it returns to its original orientation upon closure, leading to a broad range of possible winding variations. A family of loops of particular relevance to 3D active nematics is characterized by a spatially uniform **Ω**, interpolating between two emblematic geometries: wedge-twist and pure-twist loops. In the wedge-twist loop, **Ω** makes an angle γ = π/2 with the loop normal **N** (Fig. 3B). As the disclination's tangent **t** rotates by 2π upon traveling around the loop, the angle β varies from 0 (+1/2 wedge) to π/2 (twist), to π (−1/2 wedge), then back to π/2, and finally returning to 0 (movie S9) (*27*, *28*). The pure-twist loop has **Ω** uniformly parallel to **N**, so γ = 0 and **Ω** is perpendicular to **t** (β = π/2, twist profile) at all points on the loop (Fig. 3C) (*27*, *29*). In this family of loops, the director just outside the loop, $\mathbf{n}_{out}$, is also uniform. The lack of winding of both **Ω** and $\mathbf{n}_{out}$ implies that both wedge-twist and pure-twist loops are topologically neutral (*30*, *31*).

Experimental measurements of the director field allowed us to fully characterize the topological structure of the disclination loops (Fig. 4). Analysis of the director field indicated that the distortion lines and loops have the π winding indicative of disclinations (Fig. 1, E and F), with continuous variation of β, which indicates local winding. Furthermore, most of the analyzed loops were well approximated by the family of curves where **Ω** and $\mathbf{n}_{out}$ varied little along the loop circumferences. Categorizing loops according to their γ values revealed that the entire continuous family from wedge-twist (Fig. 4, A and B) to pure-twist (Fig. 4C) was represented, with the latter being more prevalent (Fig. 4D). Structural analysis revealed topological neutrality, as all 268 experimental loops and all 94 loops extracted from hybrid lattice Boltzmann simulations carried no charge. This demonstrates that among many possible configurations, topologically neutral loops are the dominant excitation mode of 3D active nematics. The same class of loop geometries also dominated the dynamics in our numerical simulations of bulk 3D active nematics and in confined active nematics (Fig. 4, E and F) (*25*, *26*, *32*, *33*). The phenomenology observed is a direct consequence of activity-induced flows and is insensitive to backflows induced by reactive stresses. This conclusion is supported by the agreement of results from the mechanical model considered in the hybrid lattice Boltzmann method and the purely kinematic Stokes method.

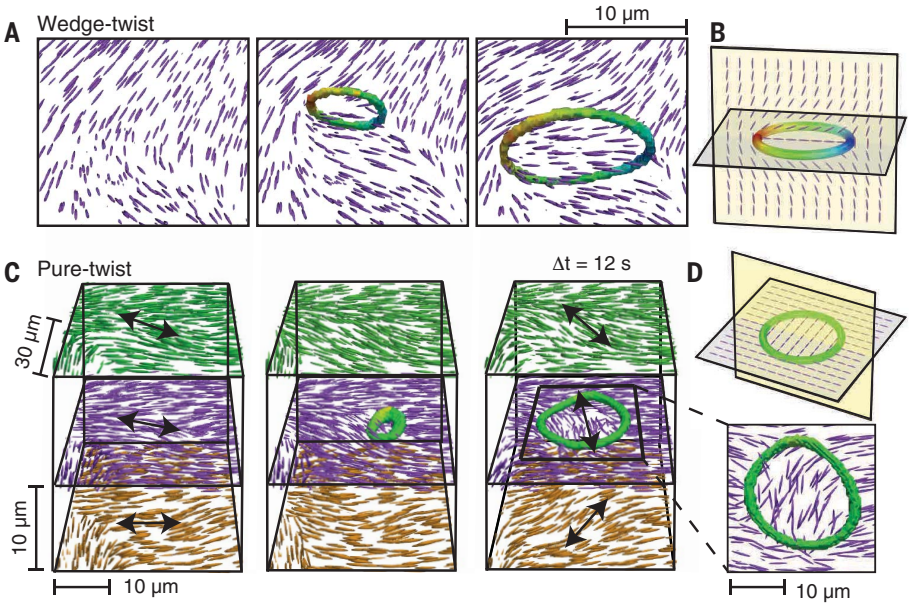

Fig. 5. Nucleation mechanism of wedge-twist and pure-twist loops. (**A**) Nucleation and growth of a wedge-twist disclination loop through a self-amplifying bend distortion. Purple rods represent the 2D director field through the local ±1/2 wedge profiles. (**B**) Schematic of a wedge-twist loop and the director field in the plane that intersects ±1/2 wedge profiles. (**C**) Pure-twist disclination loop nucleates and grows from a local twist distortion (movie S10). Black arrows indicate the local buildup of the twist distortion. Insert shows the top view of a growing twist disclination loop. (**D**) Schematic of a pure-twist loop and the director field in the loop's plane.

In 2D active nematics, self-amplifying bend distortions give rise to the nucleation of a pair of topological defects of opposite charge (*12*–*18*). Nucleation of isolated, topologically neutral wedge-twist loops are the 3D analog of the 2D defect-creation process. Specifically, a cross-section through the +1/2 and −1/2 wedge profiles recalls unbinding of a pair of point disclinations in 2D (Fig. 5, A and B). The +1/2 wedge profile typically appears on the side of the growing bend distortion, oriented away from the −1/2 wedge profile. Similarly, wedge-twist loops with the +1/2 wedge profile oriented inward toward the −1/2 wedge are driven to shrink by active and passive stresses. Unlike in 2D active nematics, after nucleation, the wedge profiles remain bound to each other through a disclination loop that includes points with a local twist winding. It is possible that some analyzed pure-twist loops have evolved from wedge-twist loops by continuous deformation of local winding character. However, both simulations and experiments showed cases of loop nucleation in nearly pure-twist (γ ≈ 0) geometries from previously defect-free regions. Local active nematic stresses alone are not expected to drive growth of a pure-twist loop (Fig. 5D). One possibility is that long-range hydrodynamic flows build up twist distortions that locally relax through creation of a pure-twist loop (Fig. 5C and movie S10).

By coupling a flow field to an orientational order parameter with curvilinear topological defects, 3D active nematics display dynamics even more complex than the chaotic flows of 2D active systems. Combined with emerging theoretical work (*32*, *33*), the experimental model system described herein offers a platform with which to investigate the role of topology, dimensionality, and material order in the chaotic internally driven flows of active soft matter. Furthermore, the use of a multiview light sheet imaging technique demonstrates its potential to unravel dynamical processes in diverse nonequilibrium soft materials, such as relaxation of nematic liquid crystals upon a quench or their deformation under external shear flow (*3*, *34*).

REFERENCES AND NOTES

1. S. Galtier, *Introduction to Modern Magnetohydrodynamics* (Cambridge Univ. Press, ed. 1, 2016).
2. C. Blanch-Mercader *et al*., *Phys. Rev. Lett.* **120**, 208101 (2018).
3. M. J. Bowick, L. Chandar, E. A. Schiff, A. M. Srivastava, *Science* **263**, 943–945 (1994).
4. P. Poulin, H. Stark, T. C. Lubensky, D. A. Weitz, *Science* **275**, 1770–1773 (1997).
5. A. R. Bausch *et al*., *Science* **299**, 1716–1718 (2003).
6. W. T. Irvine, V. Vitelli, P. M. Chaikin, *Nature* **468**, 947–951 (2010).
7. M. W. Scheeler, W. M. van Rees, H. Kedia, D. Kleckner, W. T. M. Irvine, *Science* **357**, 487–491 (2017).
8. A. Martinez *et al*., *Nat. Mater.* **13**, 258–263 (2014).
9. U. Tkalec, M. Ravnik, S. Čopar, S. Žumer, I. Muševič, *Science* **333**, 62–65 (2011).
10. R. Aditi Simha, S. Ramaswamy, *Phys. Rev. Lett.* **89**, 058101 (2002).
11. D. Marenduzzo, E. Orlandini, M. E. Cates, J. M. Yeomans, *Phys. Rev. E Stat. Nonlin. Soft Matter Phys.* **76**, 031921 (2007).
12. S. Shankar, S. Ramaswamy, M. C. Marchetti, M. J. Bowick, *Phys. Rev. Lett.* **121**, 108002 (2018).
13. L. Giomi, M. J. Bowick, P. Mishra, R. Sknepnek, M. Cristina Marchetti, *Philos. Trans. A Math. Phys. Eng. Sci.* **372**, 20130365 (2014).
14. T. Gao, R. Blackwell, M. A. Glaser, M. D. Betterton, M. J. Shelley, *Phys. Rev. Lett.* **114**, 048101 (2015).
15. S. P. Thampi, R. Golestanian, J. M. Yeomans, *EPL* **105**, 18001 (2014).
16. X. Q. Shi, Y. Q. Ma, *Nat. Commun.* **4**, 3013 (2013).
17. T. Sanchez, D. T. Chen, S. J. DeCamp, M. Heymann, Z. Dogic, *Nature* **491**, 431–434 (2012).
18. V. Narayan, S. Ramaswamy, N. Menon, *Science* **317**, 105–108 (2007).
19. K. Kawaguchi, R. Kageyama, M. Sano, *Nature* **545**, 327–331 (2017).
20. T. B. Saw *et al*., *Nature* **544**, 212–216 (2017).
21. S. Zhou, A. Sokolov, O. D. Lavrentovich, I. S. Aranson, *Proc. Natl. Acad. Sci. U.S.A.* **111**, 1265–1270 (2014).
22. N. Kumar, R. Zhang, J. J. de Pablo, M. L. Gardel, *Sci. Adv.* **4**, eaat7779 (2018).
23. H. Li *et al*., *Proc. Natl. Acad. Sci. U.S.A.* **116**, 777–785 (2019).
24. U. Krzic, S. Gunther, T. E. Saunders, S. J. Streichan, L. Hufnagel, *Nat. Methods* **9**, 730–733 (2012).
25. G. Duclos *et al*., Experimental director field data, the code to detect and analyze the topological loops and the Stokes solver for: Topological structure and dynamics of three-dimensional active nematics, Dryad (2020); https://doi.org/10.25349/D9CS31.
26. D. Banerjee *et al*., Data from numerical simulations of topological structure and dynamics of three-dimensional active nematics. 4TU.Centre for Research Data (2020); https://doi.org/10.4121/uuid:5c8ea40a-19d5-4ecb-893a-c93f238a494c.
27. J. Friedel, P. De Gennes, *CR Acad. Sc. Paris B* **268**, 257–259 (1969).
28. T. Emeršič *et al*., *Sci. Adv.* **5**, eaav4283 (2019).
29. E. M. Terentjev, *Phys. Rev. E Stat. Phys. Plasmas Fluids Relat. Interdiscip. Topics* **51**, 1330–1337 (1995).
30. G. P. Alexander, B. G. Chen, E. A. Matsumoto, R. D. Kamien, *Rev. Mod. Phys.* **84**, 497–514 (2012).
31. S. Čopar, S. Žumer, *Proc. Royal Soc. Math. Phys. Eng. Sci.* **469**, 20130204 (2013).
32. S. Čopar, J. Aplinc, Ž. Kos, S. Žumer, M. Ravnik, *Phys. Rev. X* **9**, 031051 (2019).
33. T. N. Shendruk, K. Thijssen, J. M. Yeomans, A. Doostmohammadi, *Phys. Rev. E* **98**, 010601 (2018).
34. M. S. Lavine, A. H. Windle, *Macromol. Symp.* **124**, 35–47 (1997).

ACKNOWLEDGMENTS

We thank B. Lemma, R. Subramanian, and M. Ridilla for help in protein purification. D.A.B. acknowledges S. Čopar, S. Žumer, and M. Ravnik for helpful discussions on disclinations in 3D active nematics. **Funding:** Experimental work was supported by the U.S. Department of Energy, Office of Basic Energy Sciences, through award DE-SC0019733 (G.D., R.A., I.K., and Z.D.). G.D. and I.K. also acknowledge support from HFSP fellowships. R.A. acknowledges support from NSF-GRFP. Theoretical modeling was supported by NSF-DMR-1855914, NSF-MRSEC-1420382, and NSF-CBET-1437195 (D.A.B., M.P., M.V., Ar.B., Ap.B., M.F.H., R.A.P., and T.R.P.). Computational resources were provided by the NSF through XSEDE computing resources (MCB090163) and TU/e through the F&F computing cluster. We also acknowledge use of the Brandeis optical, HPCC, and biosynthesis facilities supported by NSF-MRSEC-1420382. D.B. was supported by FOM and NWO. V.V. was supported by the Army Research Office under grant W911NF-19-1-0268 and NSF-MRSEC (DMR-1420709). S.J.S. was supported by NIH-R00 award 5R00HD088708-05. D.A.B. thanks the Isaac Newton Institute for Mathematical Sciences for support during the program "The Mathematical Design of New Materials," supported by EPSRC grant EP/R014604/1. **Author contributions:** G.D., I.K., S.J.S., and R.A. conducted experimental research; G.D., I.K., S.J.S., R.A., M.S.P., and D.A.B. analyzed experimental and theoretical data. D.B., F.T., and V.V. developed hybrid lattice Boltzmann simulations. M.S.P., M.V., Ar.B., Ap.B., and M.F.H. developed and applied finite difference Stokes solver code. D.A.B., R.P., and T.R.P. conducted theoretical modeling and interpretation of data. G.D., V.V., Ap.B., M.F.H., D.A.B., and Z.D conceived the work. G.D., D.A.B., V.V., and Z.D. wrote the manuscript. All authors reviewed the manuscript. **Competing interests:** The authors declare no competing interests. **Data and materials availability:** Experimental director field data, the code to detect and analyze the topological loops, and the Stokes solver are available on Dryad (*25*). Lattice Boltzmann code and director generated by this code are available on REPOSITORY (*26*).

SUPPLEMENTARY MATERIALS

science.sciencemag.org/content/367/6482/1120/suppl/DC1
Materials and Methods
Supplementary Text
Figs. S1 to S4
Captions for Movies S1 to S10
References (*35*–*53*)

16 September 2019; accepted 7 February 2020
10.1126/science.aaz4547